LETTER

Untethered flight of an insect-sized flapping-wing microscale aerial vehicle

Noah T. Jafferis[1,2,3]*, E. Farrell Helbling[1,2,3], Michael Karpelson[2] & Robert J. Wood[1,2]

Heavier-than-air flight at any scale is energetically expensive. This is greatly exacerbated at small scales and has so far presented an insurmountable obstacle for untethered flight in insect-sized (mass less than 500 milligrams and wingspan less than 5 centimetres) robots. These vehicles[1–4] thus need to fly tethered to an offboard power supply and signal generator owing to the challenges associated with integrating onboard electronics within a limited payload capacity. Here we address these challenges to demonstrate sustained untethered flight of an insect-sized flapping-wing microscale aerial vehicle. The 90-milligram vehicle uses four wings driven by two alumina-reinforced piezoelectric actuators to increase aerodynamic efficiency (by up to 29 per cent relative to similar two-wing vehicles[5]) and achieve a peak lift-to-weight ratio of 4.1 to 1, demonstrating greater thrust per muscle mass than typical biological counterparts[6]. The integrated system of the vehicle together with the electronics required for untethered flight (a photovoltaic array and a signal generator) weighs 259 milligrams, with an additional payload capacity allowing for additional onboard devices. Consuming only 110–120 milliwatts of power, the system matches the thrust efficiency of similarly sized insects such as bees[7].

This insect-scale aerial vehicle is the lightest thus far to achieve sustained untethered flight (as opposed to impulsive jumping[8] or liftoff[9]).

Autonomous flight has been achieved for vehicles the size of small birds, at which scales component technologies such as motors, gears and rotary bearings are well understood[10–13]. Quadrotor microscale aerial vehicles (MAVs) (such as the Aerius from Aerix Drones; http://www.aerixdrones.com) are available with masses of approximately 10 g and with sizes similar to insect-scale MAVs (with wingspan of about 5 cm). In recent years, there has been heightened interest in developing sub-gram vehicles, in part for their predicted high manoeuvrability (based on the relative scaling of torques and inertias) and utility for applications such as environmental monitoring and navigation in confined spaces. However, as the size of an MAV is reduced, alternative actuation strategies and flexure-based mechanisms are necessary to overcome the unfavourable scaling laws that degrade electromagnetic motor performance and increase frictional losses in traditional bearings. At such micrometre scales, piezoelectrics are generally chosen as actuators[14–17], because their power density scales as l^{-1} (where l is the length of the actuator) and their oscillatory operation
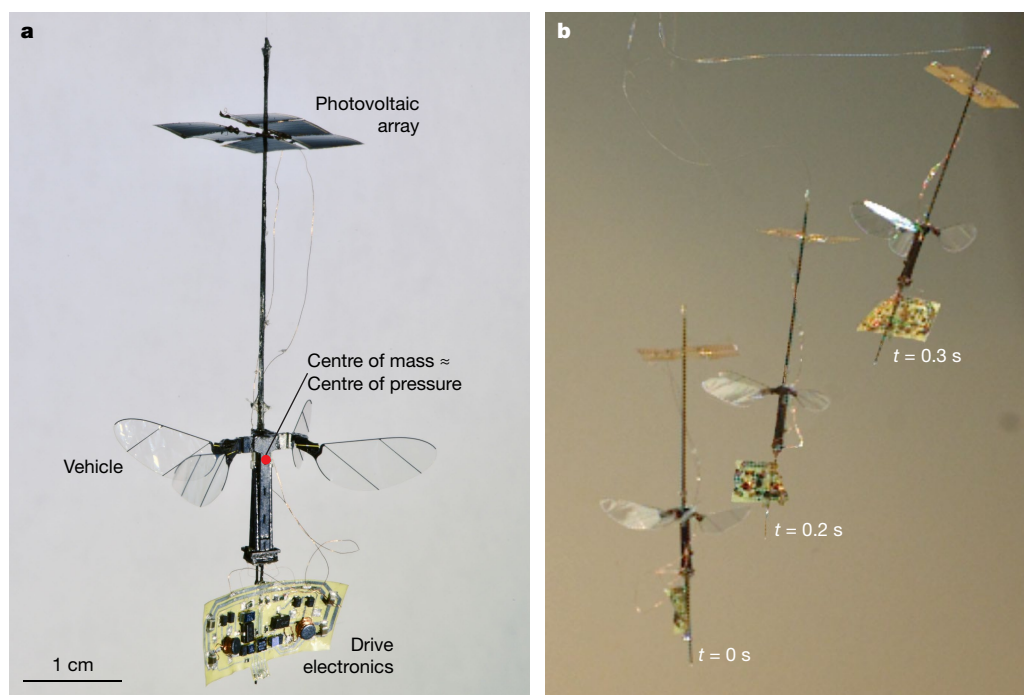

Fig. 1 | The integrated vehicle and flight performance. a, The 90-mg vehicle has four wings and a wingspan of 3.5 cm. The solar cells are positioned 3 cm above the vehicle to prevent aerodynamic interference with the wings; the drive electronics are positioned to align the centre of mass and centre of pressure. The integrated system weighs 259 mg and is 6.5 cm tall. **b,** Time-lapse video of an untethered flight (Supplementary Video 4). The light source provides a light intensity of approximately three Suns directly above the vehicle, outside the frame. The Kevlar thread attached to the solar array is to ensure vehicle safety (it provides neither current nor support during flight).

[1]John A Paulson School of Engineering and Applied Sciences, Harvard University, Cambridge, MA, USA. [2]Wyss Institute for Biologically Inspired Engineering, Harvard University, Boston, MA, USA. [3]These authors contributed equally: Noah T. Jafferis, E. Farrell Helbling. *e-mail: njafferis@seas.harvard.edu
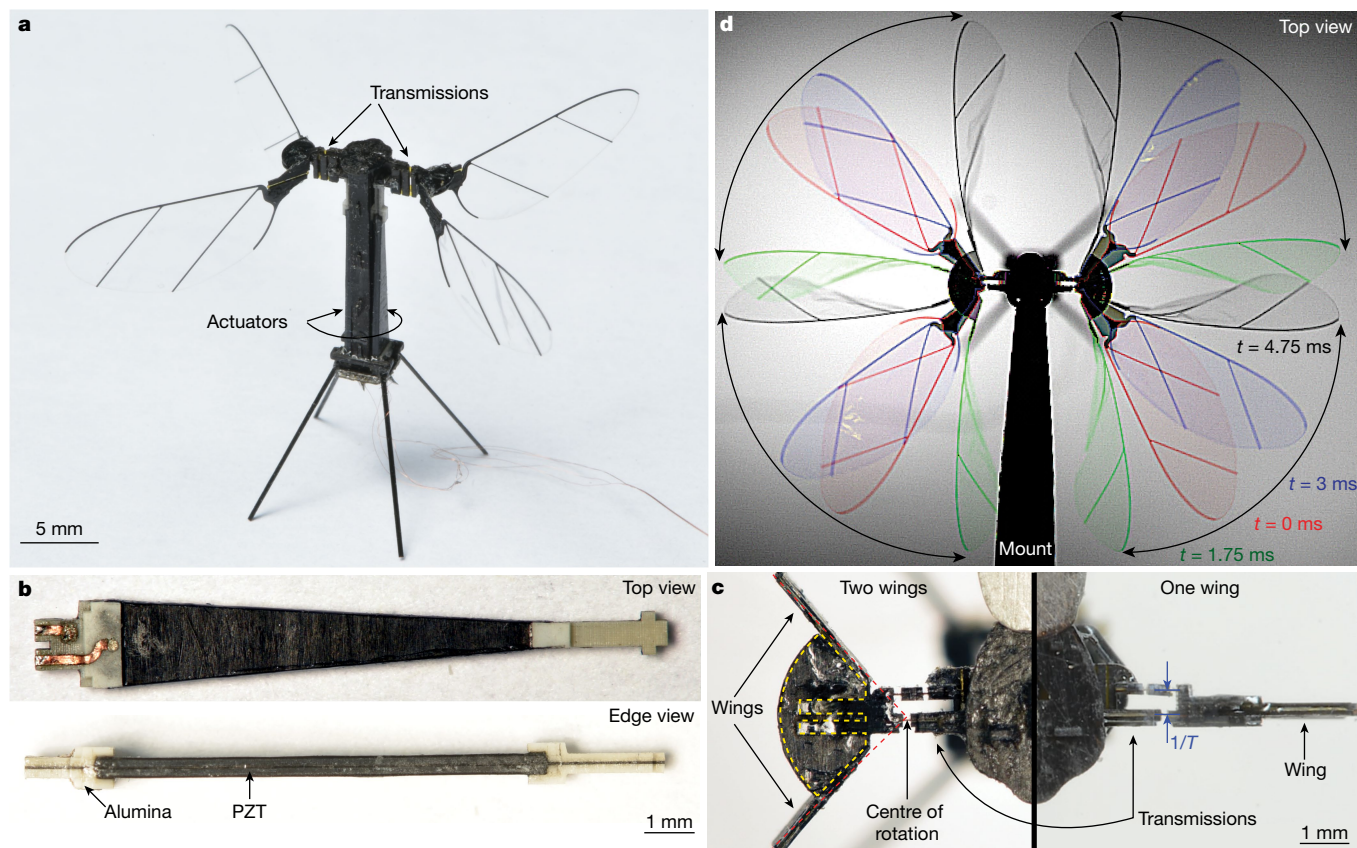
Fig. 2 | Vehicle design. a, Our vehicle, the RoboBee X-Wing. **b**, Alumina-bridge piezoelectric actuators (PZT is lead zirconate titanate). **c**, Close-up top-view of the vehicle showing the transmissions with attachment mechanisms for two wings per actuator (left; as used in **a**) versus one wing per actuator (right; as used in previous vehicles). The adaptor for affixing two wings to the transmission is outlined in yellow. The transmission ratio, T, and the centre of wing stroke rotation are also indicated. **d**, Wing kinematics time-lapse under the peak-lift operating conditions (210 V, 165 Hz). See Extended Data Table 1 and Extended Data Fig. 7 for vehicle parameters and performance, and system power and weight trade-off plots.

is well matched with the desired motion of flapping wings. Recent advances in manufacturing and assembly have further increased their power density and robustness in microrobotic applications[18]. However, such vehicles have been limited to flying tethered to an off-board power supply and control system. Here we integrate a low-mass power source and signal generator onboard an insect-scale vehicle (see Fig. 1a) to achieve sustained untethered flight (Fig. 1b). We call our vehicle the RoboBee X-Wing (Fig. 2a).

The small size of these vehicles means that custom-made, light-weight, high-efficiency power electronics are necessary to generate the high-voltage (about 200 V), time-varying (about 200 Hz) drive signals for flapping-wing propulsion. Switching topologies such as the tapped-inductor boost converter and half-bridge drive stage, the bidirectional flyback converter[19], and the charge pump ladder[20] can efficiently transfer energy from a low-voltage power source to the piezoelectric load. These topologies are also well suited to the mass (about 100 mg) and power (about 100 mW) constraints of these vehicles. Furthermore, they are drop-in compatible with any small-scale energy sources (such as batteries, capacitors and photovoltaic cells) that provide sufficient power density.

At small scales, a battery's mass is dominated by its sealing material and packaging owing to the high surface-to-volume ratio. Commercially available options include lithium-ion batteries (such as the GEB201212C from PowerStream; https://www.powerstream.com/lip/PGEB201212C.pdf) that have rated power densities of approximately 1.2 W g^{-1} (and have demonstrated >3 W g^{-1} in other small-scale autonomous vehicles)[11,21], but weigh more than four times the vehicle's mass, thus eliminating off-the-shelf batteries from practical consideration. Recent developments in manufacturing custom-made, lightweight lithium-ion batteries have produced batteries with power densities comparable to those of commercial batteries[22]. However, these have not yet demonstrated sufficient power density in sub-100-mg packages. Solar cells, however, offer a promising alternative, and have been used in a number of autonomous vehicles[23–25]. Commercially available 10-mg devices (TSC-E-3J-AA-0.25-B0 from MicroLink Devices; http://mldevices.com/index.php/product-services/photovoltaics) can provide power densities of about 2.3 W g^{-1} at 3 Suns (where 1 Sun ≈ 1 kW m^{-2}).

Given the lift, weight, power and efficiency of the state-of-the-art vehicles[5], drive electronics[19] and power supply, untethered flight would require impractically high light intensities of around 5 to 7 Suns (see Methods for an analysis of the system weight and power trade-offs). We address this with a new vehicle design (Fig. 2a). First, improvements to the actuator design (Fig. 2b; see Methods) and a reduction in the transmission ratio (the ratio of the wing stroke angle to the actuator tip deflection) provide a 38% increase in peak lift (without changing actuator size). To achieve this dramatic increase in lift force without substantially increasing power, we leverage the fact that power is force times velocity by flapping a larger area of wings more slowly. The most effective way to increase wing area is to add more wings (Fig. 2c), with a four-wing vehicle able to increase efficiency by up to 30% (see Methods, Extended Data Fig. 7, and Extended Data Table 1b for a detailed analysis). Similarly sized vehicles have used four wings to increase lift, but at the expense of proportionately increased vehicle mass and power[26]. At a larger scale, multi-wing vehicle designs have also been used to explore alternative flapping strategies, such as clap-and-fling[13,27].

These changes to system parameters (that is, transmission ratio, lift and drag forces, and number of wings) are accompanied by corresponding changes to the wing inertia and stiffness and the wing hinge
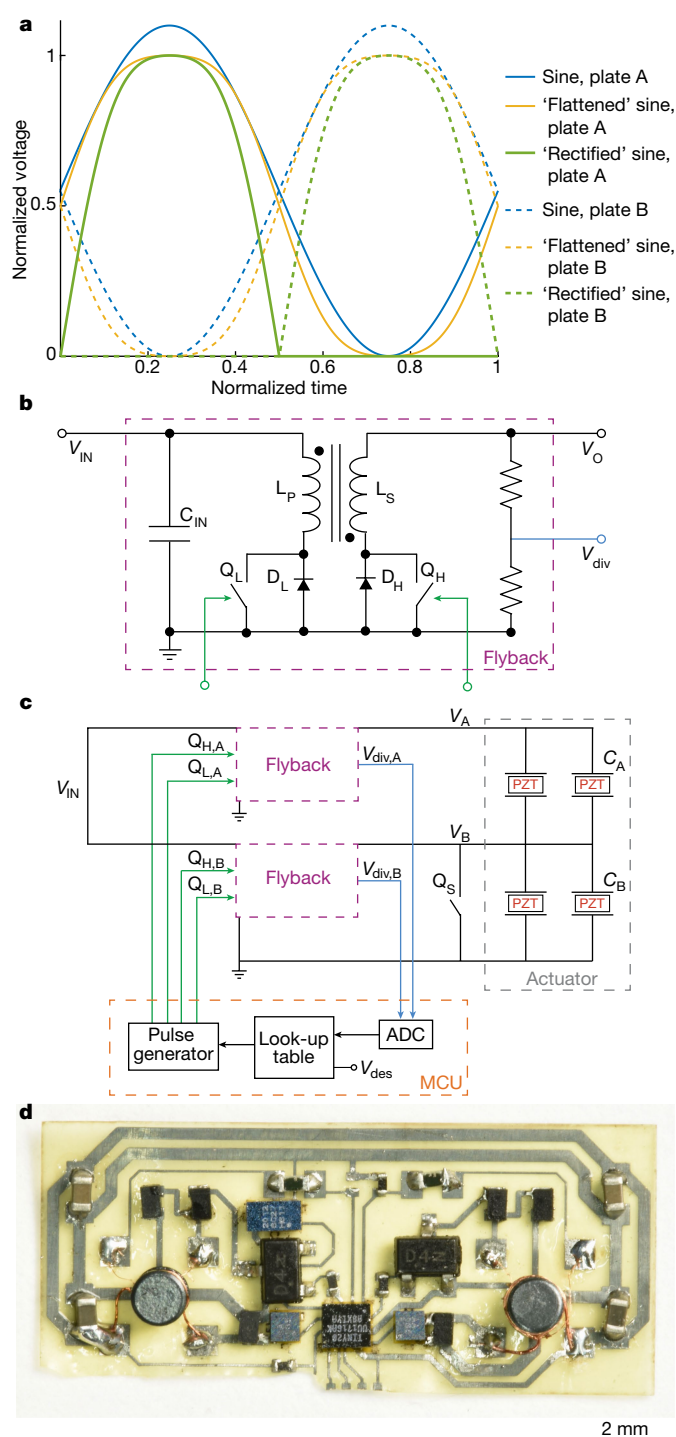
stiffness. This is done to maintain the mean lift-to-drag ratio of the wings (for example, by keeping the same stroke and pitch resonant frequencies and maintaining experimentally observed wing torsion). The details of these changes are described in Methods (and Extended Data Table 1a).

The final four-wing vehicle design (Fig. 2a) has a wingspan of 3.5 cm, weighs 90 mg, and can generate a peak lift of 370 mg for a lift-to-weight ratio of 4.1:1 (Supplementary Videos 1 and 2, and kinematics in Fig. 2d). The final vehicle performs within 10% of predictions at the operating conditions of interest (190–210 V and 165–173 Hz; see Extended Data Table 1b and Methods for full performance details), and provides the first viable platform with which to demonstrate untethered flight at this scale.

It is important to optimize the drive signals to reduce power consumption and minimize the mass and complexity of the drive electronics. In particular, we use non-sinusoidal waveforms to reduce the required peak-to-peak voltages by 10% (see Fig. 3a and Methods). This takes advantage of the vehicle's flapping dynamics, which strongly filter out frequencies above resonance. Additionally, we implement a drive scheme that powers only one plate of a bimorph actuator at a time, which ensures that zero output force corresponds to zero voltage (Fig. 3a). This minimizes the actuator's power consumption and stress, and reduces the number of control signals, simplifying the control architecture and allowing for a smaller microcontroller. To greatly reduce the circuit mass and complexity, the two actuators share drive signals, thus halving the number of components.

Our custom power electronics, using a bidirectional flyback topology (selected for minimal components and lower mass), consist of off-the-shelf discrete components and custom-wound transformers and convert the low-voltage input signal (4.8 V) from photovoltaic cells to the approximately 200-V and 170-Hz signals necessary to drive the actuators. The two piezoelectric actuators consume about 26–35 mW real power (IV) and about 50–59 mW reactive power (CV^2f) (where I, V, C and f are the actuator's current, voltage, capacitance and frequency, respectively; see Methods for further details).

A schematic for the circuit design and the control architecture can be seen in Fig. 3b, c. We use one analogue-to-digital converter (ADC) for the two plates of the bimorph and carefully multiplex the charge and discharge pulses for the first plate 'plate A', and then the second plate, 'plate B'. For either plate, the output voltage, V_A or V_B, is sampled through the ADC and compared with a digital control signal (V_{des}, the desired value of the output voltage). During the charge phase, a pulse is issued to switch Q_L if the output is below V_{des}. During the discharge phase, a pulse is similarly issued to switch Q_H if the output is above V_{des}. The on times for Q_L and Q_H can be determined using standard inductor equations, described in detail in previous work[19]. As seen in Fig. 3c, the circuit requires an additional switch (Q_S) on the output of plate B, V_B. This electrically clamps plate B to ground while plate A is charged and discharged. When plate B is charged and discharged, the output of plate A, V_A, is not actively driven and is allowed to rise with plate B to prevent depoling of the actuator (see Extended Data Fig. 5).

The physical instantiation of the circuit can be seen in Fig. 3d. It weighs 91 mg and consumes, on average, 110–120 mW to drive the piezoelectric load at the experimentally determined operating conditions for untethered flight (193 V, 174 Hz). To ensure that quantization effects from the discrete timing of the microcontroller do not noticeably affect propulsion, we compared the flapping kinematics using a high-speed camera (Vision Research version 7.3) when the actuator signals (nomenclature shown in Fig. 4a) were provided by off-board signal generators (the xPC Target from MathWorks and the PZD350A from Trek) and the custom power electronics (Supplementary Video 3). The recorded signal from the power electronics can also be seen in Fig. 4b, compared to an idealized waveform. The quantization has a minimal effect on the flapping kinematics, and a fast Fourier transform (Fig. 4d) confirms that the signals are nearly identical in the first harmonic.

Because identical signals are sent to both actuators, we have no onboard control with which to minimize any torque biases (for
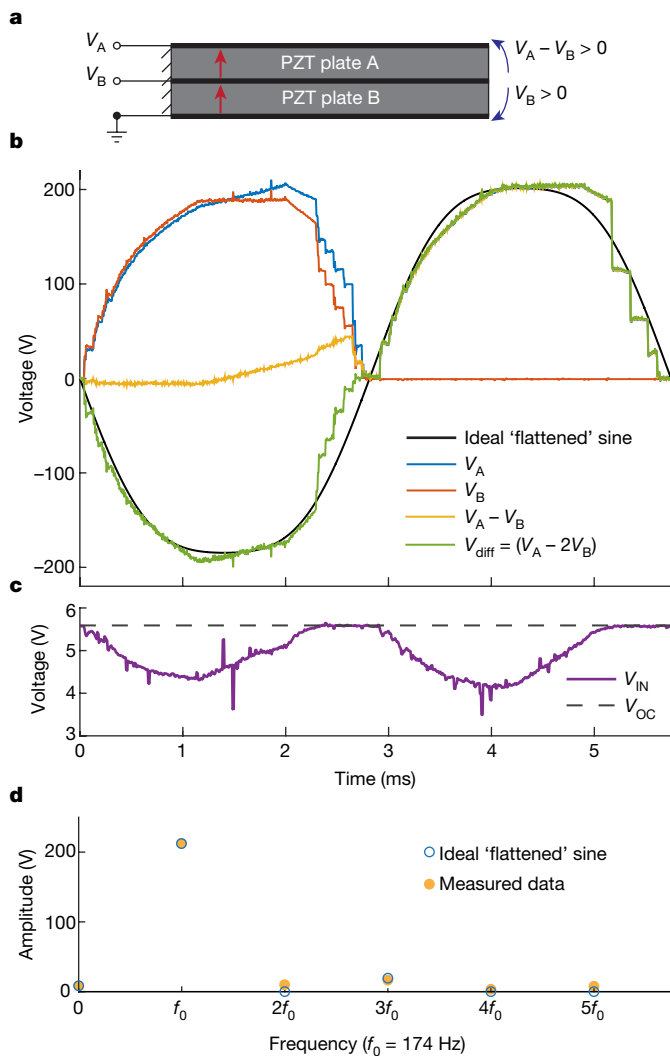
Fig. 3 | Drive electronics. a, Three drive waveforms that result in identical flapping kinematics (see Methods for details of drive waveforms). **b**, Circuit diagram of a bidirectional flyback converter. V_{IN} is the input voltage, C_{IN} is the input capacitor, Q_L is the low-side switch, D_L is the low-side diode, L_P is the primary winding of the transformer, L_S is the secondary winding of the transformer, Q_H is the high-side switch, D_H is the high-side diode and V_O is the output voltage. **c**, Full circuit diagram, including two bidirectional flyback converters from **b** (purple), driving two piezoelectric bimorphs (labelled 'Actuator'). One ADC in the microcontroller unit (MCU) (orange) monitors the output voltage of plate A (V_A) or plate B (V_B) using the corresponding low voltages $V_{div,A}$ or $V_{div,B}$, respectively; a look-up table compares the result to a desired voltage V_{des} and generates a corresponding pulse to switches $Q_{H,A}$, $Q_{L,A}$, $Q_{H,B}$ and $Q_{L,B}$. The additional switch Q_S electrically clamps plate B to ground when plate A is driven. C_A and C_B are the capacitances of the actuator plates. **d**, Physical instantiation of **c**.

a

b

c

d

Fig. 4 | Measured drive signals. a, Actuator cross-sectional diagram, indicating voltage nomenclature, polarization direction (red arrows), and bending directions (blue arrows). **b**, Measured voltages applied to the vehicle (see nomenclature from **a**; V_{diff} is the voltage difference between the plates). An idealized flattened sine ($V_{pp} = 193$ V, $f = 174$ Hz; an 8.4-V offset is added to match the data—see Methods) is plotted for comparison. **c**, The corresponding input voltage (V_{IN}); V_{OC} is the open-circuit voltage of the photovoltaic array. **d**, The magnitudes of the first few harmonics for the measured data (V_{diff}) and the idealized flattened sine are compared.

example, from fabrication asymmetries), which are often seen during open-loop (uncontrolled) flight. With minimal onboard control authority, researchers have investigated the use of sails for passive stability[27,28]. In this work, we implement an alternative approach for sustained upward flight that involves (1) careful matching and assembly of all components in the vehicle to minimize inherent torque biases, (2) ensuring that we have a lift force approximately 10% greater than the entire system mass, and (3) bringing the vertical position of the centre of mass of the system in line with the centre of pressure of the wings (see Methods). The solar cell array has a sizeable area, and is placed 3 cm above the top of the vehicle to prevent the array from interfering with the airflow from the flapping wings[29]. With this positioning fixed, we can then place the circuit board to achieve the desired centre of mass position (Fig. 1a). The integrated vehicle has a wingspan of 3.5 cm and is 6.5 cm tall.

For the untethered flights, we chose to operate at a relatively low voltage (193 V) to improve the lifetime of the vehicle during testing, ensure repeatability in experiments, and remain within the voltage rating of some discrete components. Although the choice of energy

source does not change the topology of the signal generator, at this operating condition (193 V) the vehicle has less than 100 mg available for a power supply. We therefore selected a 60-mg photovoltaic array with a light source of about 3 Suns. We provide a peak power of at least 150 mW (see Methods), and the integrated vehicle successfully takes off and performs sustained upright flights (Fig. 1b and Supplementary Videos 4 and 9). The vehicle demonstrates a lift of 290 mg under these conditions (see Methods).

To put these results in context, we note that the smallest quadcopters (such as the Aerix quadrotor) have a similar wingspan to our vehicle, weigh approximately 7 g, can achieve stable flight for approximately five minutes, and consume approximately 3 W for a lift-to-power ratio of 2.3. Although the vehicle presented here has a substantially smaller payload and cannot integrate all necessary components for onboard control, it achieves a comparable lift-to-power ratio of 2.4 with approximately 25 times lower mass and power. This provides several advantages, including the ability to obtain its power from photovoltaic cells and perch on fragile/flexible surfaces during future outdoor experiments. In addition, vehicles with very low masses (of the order of several hundred milligrams or less) have extremely low kinetic energy during flight. This implies greater safety—both for the vehicles and the environments they operate in—compared to heavier drones.

The achievements described in this work represent a major milestone in the development of autonomous insect-scale flying vehicles. Through a system-level design exploration, the use of two pairs of wings, and the creation of ultra-compact signal-generation electronics, we have demonstrated sustained untethered flight of a robotic insect. Additionally, our vehicle has an extra payload capacity of approximately 70 mg with which to carry lightweight sensors[30,31], control electronics[32] or a larger power supply (for example, larger solar arrays or a battery[22]) for future autonomous operation. Further vehicle improvements and continued system-level exploration are expected to enable continuous outdoor flight. These improvements include using multilayer actuators[33] to halve the actuation voltage and increase drive circuit efficiency, incorporating a blocking diode to allow energy recovery (Fig. 4c; Methods), configuring the actuators for alternating drive[19] to reduce circuit components and increase efficiency, increasing the vehicle size (see Methods for a detailed analysis of system trade-offs), and investigating potential wing–wing interactions to determine the optimal wing spacing and number of wings.

Online content

Any Methods, additional references, Nature Research reporting summaries, source data, statements of data availability and associated accession codes are available in the online version of the paper at https://doi.org/10.1038/s41586-019-1322-0.

1. Ma, K. Y., Felton, S. M. & Wood, R. J. In *IEEE Int. Conf. on Intelligent Robots and Systems (IROS)* 1133–1140 (IEEE/RSJ, 2012).
2. Zou, Y., Zhang, W. & Zhang, Z. Liftoff of an electromagnetically driven insect-inspired flapping-wing robot. *IEEE Trans. Robot.* **32**, 1285–1289 (2016).
3. Balasubramanian, S., Chukewad, Y. M., James, J. M., Barrows, G. L. & Fuller, S. B. An insect-sized robot that uses a custom-built onboard camera and a neural network to classify and respond to visual input. In *7th IEEE Int. Conf. on Biomedical Robotics and Biomechatronics (Biorob)* 1297–1302 (IEEE, 2018).
4. Drew, D. S. & Pister, K. S. In *IEEE Int. Conf. on Manipulation, Automation and Robotics at Small Scales (MARSS)* 1–5 (IEEE, 2017).
5. Jafferis, N. T., Graule, M. A. & Wood, R. J. In *2016 IEEE Int. Conf. on Robotics and Automation (ICRA)* 3234–3241 (IEEE, 2016).
6. Marden, J. H. Maximum lift production during takeoff in flying animals. *J. Exp. Biol.* **130**, 235–258 (1987).
7. Nachtigall, W., Hanauer-Thieser, U. & Mörz, M. Flight of the honey bee. VII: Metabolic power versus flight speed relation. *J. Comp. Physiol. B* **165**, 484–489 (1995).
8. Churaman, W. A., Currano, L. J., Morris, C. J., Rajkowski, J. E. & Bergbreiter, S. The first launch of an autonomous thrust-driven microrobot using nanoporous energetic silicon. *J. Microelectromech. Syst.* **21**, 198–205 (2012).
9. James, J., Iyer, V., Chukewad, Y., Gollakota, S. & Fuller, S. B. In *IEEE Int. Conf. on Robotics and Automation (ICRA)* 1–8 (IEEE, 2018).
10. Keennon, M., Klingebiel, K. & Won, H. In *50th AIAA Aerospace Sciences Meeting including the New Horizons Forum and Exposition* 588 (AIAA, 2012).

11. Rosen, M. H., le Pivain, G., Sahai, R., Jafferis, N. T. & Wood, R. J. In *IEEE Int. Conf. on Robotics and Automation (ICRA)*. 3227–3233 (IEEE, 2016).
12. de Croon, G., de Clercq, K., Ruijsink, R., Remes, B. & de Wagter, C. Design, aerodynamics, and vision-based control of the delfly. *Int. J. Micro Air Veh.* **1**, 71–97 (2009).
13. Karásek, M., Muijres, F. T., de Wagter, C., Remes, B. D. & de Croon, G. C. A tailless aerial robotic flapper reveals that flies use torque coupling in rapid banked turns. *Science* **361**, 1089–1094 (2018).
14. Hines, L. Design and Control of a Flapping Flight Micro Aerial Vehicle. PhD thesis, Carnegie Mellon Univ. (2014); https://www.ri.cmu.edu/publications/design-and-control-of-a-flapping-flight-micro-aerial-vehicle/.
15. Steltz, E., Avadhanula, S. & Fearing, R. S. In *IEEE Int. Conf. on Intelligent Robots and Systems (IROS)* 3987–3992 (IEEE/RSJ, 2007).
16. Anderson, M. L. Design and Control of Flapping Wing Micro Air Vehicles. PhD thesis, Air Force Institute of Technology Wright-Patterson AFB OH School of Engineering and Management (2011); https://apps.dtic.mil/docs/citations/ADA549053.
17. Smith, G. L. et al. PZT-based piezoelectric MEMS technology. *J. Am. Ceram. Soc.* **95**, 1777–1792 (2012).
18. Jafferis, N. T., Smith, M. J. & Wood, R. J. Design and manufacturing rules for maximizing the performance of polycrystalline piezoelectric bending actuators. *Smart Mater. Struct.* **24**, 065023 (2015).
19. Karpelson, M., Wei, G.-Y. & Wood, R. J. Driving high voltage piezoelectric actuators in microrobotic applications. *Sens. Actuators A* **176**, 78–89 (2012).
20. Steltz, E., Seeman, M., Avadhanula, S. & Fearing, R. S. In *Int. Conf. on Intelligent Robots and Systems* 1322–1328 (IEEE/RSJ, 2006).
21. Goldberg, B. et al. Power and control autonomy for high-speed locomotion with an insect-scale legged robot. *IEEE Robot. Autom. Lett.* **3**, 987–993 (2018).
22. Duduta, M., de Rivaz, S., Clarke, D. R. & Wood, R. J. Ultralightweight, high power density lithium-ion batteries. *Batteries Supercaps* **1**, 131–134 (2018).
23. Brühwiler, R. et al. In *Int. Conf. on Intelligent Robots and Systems* 5727–5733 (IEEE/RSJ, 2015).
24. Hollar, S., Flynn, A., Bellew, C. & Pister, K. In *16th Ann. Int. Conf. on Micro Electro Mechanical Systems (MEMS-03)* 706–711 (IEEE, 2003).
25. Boucher, R. J. Sunrise, the world's first solar-powered airplane. *J. Aircr.* **22**, 840–846 (1985).
26. Fuller, S. B. Four wings: an insect-sized aerial robot with steering ability and payload capacity for autonomy. *IEEE Robot. Autom. Lett.* **4**, 570–577 (2019).
27. van Breugel, F., Regan, W. & Lipson, H. From insects to machines. *IEEE Robot. Autom. Mag.* **15**, 68–74 (2008).
28. Teoh, Z. E. et al. In *Int. Conf. on Intelligent Robots and Systems* 3209–3216 (IEEE/RSJ, 2012).
29. Graule, M., et al. Perching and takeoff of a robotic insect on overhangs using switchable electrostatic adhesion. *Science* **352**, 978–982 (2016).
30. Fuller, S. B., Helbling, E. F., Chirarattananon, P. & Wood, R. J. Using a MEMS gyroscope to stabilize the attitude of a fly-sized hovering robot. In *International Micro Air Vehicle (IMAV) Conference and Competition* (Delft University of Technology (TU Delft), 2014).
31. Helbling, E. F., Fuller, S. B. & Wood, R. J. In *Robotics Research* 57–69 (Springer, 2018).
32. Zhang, X. et al. In *IEEE Symp. on VLSI Circuits C152–C153* (IEEE, 2015).
33. Jafferis, N. T., Lok, M., Winey, N., Wei, G.-Y. & Wood, R. J. Multilayer laminated piezoelectric bending actuators: design and manufacturing for optimum power density and efficiency. *Smart Mater. Struct.* **25**, 055033 (2016).

Additional information
Extended data is available for this paper at https://doi.org/10.1038/s41586-019-1322-0.
Supplementary information is available for this paper at https://doi.org/10.1038/s41586-019-1322-0.
Reprints and permissions information is available at http://www.nature.com/reprints.
Correspondence and requests for materials should be addressed to N.T.J.
Publisher's note: Springer Nature remains neutral with regard to jurisdictional claims in published maps and institutional affiliations.

METHODS

Vehicle design. The vehicle described in this paper has undergone several important design changes relative to previous vehicles. The most notable of these changes involves the use of four wings instead of two (to increase efficiency), and a reduced transmission ratio, T (to increase lift). In this subsection, we describe how to adjust T and a variety of other system properties to enable the switch from two wings to four, under the conditions of fixed input power, actuator lifetime and voltage.

First, we note that the transmission acts as a lever, so reducing T results in a greater force available at the wing ($F_{wing} \propto 1/T$)—see Methods section 'System analysis' below for an explanation of why this is preferable to increasing the voltage or the actuator width. To determine the required change in T (while satisfying our fixed-voltage condition), we equate the increase in F_{wing} to the increase in lift and drag forces caused by adding more wings ($F_{L,D} \propto N\upsilon^2$, where N is the number of wings and υ is the stroke velocity):

$$T_{old}/T_{new} = (N_{new}/N_{old})(\upsilon_{new}/\upsilon_{old})^2 \qquad (1)$$

This estimate neglects any aerodynamic wing interactions and assumes that we can adjust all other vehicle parameters (for example, wing hinge stiffness) to maintain the desired wing kinematics (that is, the maximum wing pitch and the phase between wing pitch and wing stroke). To satisfy our conditions of fixed input power and actuator lifetime, we must also hold the stroke resonant frequency f_s and actuator strain ϵ constant. With these constraints, $\upsilon \propto \Phi f_s \propto \Phi$ (where Φ is the stroke angle amplitude) and $\Phi \propto \epsilon T \propto T$, which implies that $\upsilon \propto T$. Plugging this into equation (1) results in:

$$T_{new} = 2^{-1/3}T_{old} \approx T_{old}/1.26 \qquad (2)$$

These changes to T and N necessitate corresponding changes to each wing's pitch and stroke inertia ($I_{xx,tot}$ and $I_{yy,tot}$) and stiffness, wing hinge stiffness (κ_{wh}), and transmission/actuator stiffness (K_{tot}) in order to maintain performance (that is, an effective lift-to-drag ratio). Complicating matters is the fact that the wings are generally not rigid plates, but rather undergo considerable torsion and some span-wise bending. Optimization of this effect is outside the scope of this work, so here we focus on maintaining any such deformations as we change from two wings to four. Ideally, we would like to make the following changes: (1) multiply all wing-related stiffnesses (that is, κ_{wh} and the wing's out-of-plane, in-plane and torsional stiffnesses) by $(T_{old}/T_{new})/(N_{new}/N_{old}) = 0.63$ to match the expected drop in lift and drag forces per wing; (2) multiply $I_{xx,tot}$ by the same factor to maintain the wing-pitch resonant frequency ($f_p \propto (\kappa_{wh}/I_{xx,tot})^{0.5}$); (3) increase the transmission stiffness (κ_T) and/or actuator stiffness (K_{act}) to maintain the total system stiffness ($K_{tot} = K_{act} + \kappa_T T^2$); and (4) multiply $I_{yy,tot}$ by $(T_{old}/T_{new})^2(N_{old}/N_{new}) = 0.79$ to maintain f_s (which is proportional to $(K_{tot}/(I_{yy,tot} N T^2))^{0.5}$).

In practice, it is challenging to implement all of these changes without redesigning the relative dimensions of the wing spars and leading edge and/or using materials with higher specific modulus (except in situations where the wings are closer to rigid plates, which eliminates several of the requirements). Additionally, there is a discrete set of available thicknesses for the carbon fibre composites that we use to construct the wings. We therefore made the following compromises in our new vehicle design (Extended Data Table 1a details these parameter changes, as compared to a previous two-wing vehicle[5], henceforth referred to as 'SDAB1'): (1) we reduce the width w of the wings' leading edge and spars by 25% and maintain their thickness, which reduces $I_{xx,tot}$ and $I_{yy,tot}$ by approximately 20% (the unchanged membrane is estimated to comprise 20%–25% of the inertia); (2) we reduce κ_{wh} by 25%, which results in a 3% drop in the expected f_p; and (3) we increase K_{act} and keep M_{eff} fixed to obtain a 7% drop in K_{tot}, and thus a 3%–4% drop in f_s.

Finally, we note that reducing the transmission ratio can only increase the available force if the actuators have sufficiently rigid mechanical grounding. This was a limiting factor for the actuators[18] used in SDAB1. To address this, we introduce a new actuator design that utilizes micro-machined alumina (Fig. 2b and Extended Data Fig. 1) to eliminate the weakest bonds within the actuator. The alumina thickness is chosen to ensure that it resists bending even if the remaining alumina-to-PZT bond fails (the bond of the PZT and alumina to the central carbon fibre has a much larger area, and was not a limiting factor).

Vehicle performance. We analyse the performance of the new vehicle with a series of bench-top tests to verify the wing kinematics and system frequency response. This enables us to determine the ideal operating conditions (that is, resonant frequency) for several voltages (190 V, 200 V and 210 V). The range of voltages is chosen to ensure that sufficient lift is available for untethered flight, and to determine the maximum additional payload capacity, while keeping the actuator strain similar to that of previous vehicles. The kinematics at the 210 V, 165 Hz resonance are shown in Fig. 2c (see Supplementary Videos 1, 5 and 6 for kinematics at several operating conditions).

We then add dummy weights to the vehicle, and perform open-loop flights at these resonant conditions (see Supplementary Videos 2, 7 and 8). Measuring the

vertical acceleration during these flights allows us to determine the lift force. We use this method because it is more accurate than the available force sensors. As an example, Extended Data Fig. 2 shows the vertical trajectory of the vehicle at the peak lift (210 V, 165 Hz) operating condition, while carrying a 245-mg payload. The vertical acceleration of the vehicle calculated from this plot shows that its lift is 370 mg at this operating condition.

We can also estimate the change in effective mean lift-to-drag ratio of the wings (an important metric for determining how well we matched the wing kinematics to that of the previous vehicle, SDAB1) as follows: the effective lift coefficient, $C_{l,eff}$ is defined as:

$$\frac{F_l}{0.5\rho_{air}NA_w(2\pi f\Phi R_{cp})^2}$$

(derived from standard lift and drag expressions), where F_l is the lift generated, N is the number of wings, A_w is the wing area, and R_{cp} is the distance from wing root to the centre of pressure of the wing. Similarly, the effective drag coefficient, $C_{d,eff}$ is defined as:

$$\frac{F_d}{0.5\rho_{air}NA_w(2\pi f\Phi R_{cp})^2}$$

If we operate at resonance, the drag force is balanced by the actuator force, that is, $F_{act} = F_d R_{cp} T$. Also, F_{act} is proportional to the voltage, V. Thus, the change in $C_{l,eff}$ is computed from the measured changes in F_l, f, Φ and N, while the change in $C_{l,eff}$ is computed from the measured changes in V, T, f, Φ and N.

Finally, we compare our experimental results with our model predictions. Extended Data Table 1b shows the results of these characterizations. For example, under equivalent strain conditions, we achieve the expected 26% increase in lift compared with our two-wing vehicle, SDAB1 (it increased from 270 mg to 340 mg). The effective drag is about 10% higher than expected, which means that we need to use a voltage about 10% higher than expected. This could be the result of several factors, including: (1) imperfect matching of the system parameters (for example, since we could not scale all of the stiffnesses and inertias exactly as desired), which would effectively mean that we are not operating precisely under the conditions at which the wing drag balances the actuator force; (2) vehicle variations (even two nominally identical vehicles can vary by a few per cent in performance; see Extended Data Table 1b); (3) the wing hinge being too stiff; (4) the possible effect of reduced stroke amplitude (that is, separately from the stroke speed); and/or (5) unfavourable interactions between wings. Interestingly, at a slightly higher voltage (210 V), we see an improvement in the effective lift-to-drag ratio. Here it is only about 5% less than expected, which is consistent with assumptions (1), (3) and (4) above. We may also be seeing some favourable wing interactions at this higher stroke amplitude that counteract whatever is causing the loss at the lower stroke amplitudes. Future work that focuses on the fluid dynamics of these wing–wing interactions should shed light on this issue.

Although demonstrating full control of this vehicle (for example, by showing that the vehicle can hover) is outside the scope of this work, we note that the implementation of pitch, roll and yaw torques are the same in this vehicle as for a two-wing vehicle (Extended Data Fig. 3). We show that the vehicle is capable of executing pitch and roll by mounting it in different orientations on a magnetic pin that is free to rotate about either the pitch or roll axes, and applying open-loop torque commands identical in form to those used in previous two-wing vehicles[1] (see Supplementary Video 10). Although the four-wing vehicle used for this test was partly damaged, a simple analysis of its angular accelerations in these videos (the vehicle's inertia is estimated to be >20 g mm^{-2}) suggests pitch and roll torques of approximately 1 μN m (this is a lower bound, since there is non-negligible drag, friction and/or inertial coupling that act to resist the rotation of the vehicle), which is similar to that obtained for the two-wing vehicle[1]. A detailed quantification of the torque capabilities of the vehicle is left for future work.

Drive waveform. While extreme flattening of the drive signal leads to a square wave, and the lowest possible peak-to-peak voltage for a given first harmonic, this could cause actuator failure owing to the higher stresses that the piezoelectric plates would experience during sharp transitions in the drive signal. Hence, we take a conservative approach, and add only the third harmonic, which results in a 10% lower peak-to-peak voltage (V_{pp}) for the same first harmonic (that is, $V(t) = 0.5V_0 + 1.1V_0\sin(2\pi ft) + 0.1V_0\sin(6\pi ft)$ has $V_{pp} = V_0$ and a first harmonic of $1.1V_0$). Further, owing to the direct-current offset in our unipolar drive scheme, this flattening results in a waveform whose value is always lower than the regular sine with the same first harmonic (Fig. 3a). Although this drive scheme does not reduce the real power consumption (IV), it reduces the apparent capacitive load (CV^2f), and the lower voltage increases the efficiency of the drive electronics. When we drive only one plate at a time (referred to as the 'rectified' sine in Fig. 3a), the equations for the drive signals

are $V_{B,A-B}(t) = \max\{0, \pm 2[1.1V_0\sin(2\pi ft) + 0.1V_0\sin(6\pi ft)]\}$ (see Fig. 4a for drive signal nomenclature). The total force produced by the actuator is determined from the difference in voltage across the two plates, $V_{diff} = (V_A - V_B) - V_B = -2[1.1V_0\sin(2\pi ft) + 0.1V_0\sin(6\pi ft)]$.

Power supply. The solar cells (TSC-E-3J-AA-0.25-B0 from MicroLink Devices) are individually characterized by the supplier, which allows us to choose cells where performance is near the mean of the batch (7.6 mW at 1 Sun (1 kW m⁻²); weight 9–10 mg). We wire six of these cells together, three in parallel, with two sets of three in series (Extended Data Fig. 4a). The structure supporting the solar cell array is an obelisk-shaped post consisting of three 4-cm-long strips of carbon fibre composite, and weighs <4 mg.

To produce a light intensity of several Suns, we use a combination of halogen (PALLITE VIII from SciTech) and LED lights (900590P from Visual Instrumentation). This is necessary because the solar cells are triple junction and require radiation over their full absorption spectrum; the LED lights provide the short wavelengths (around 420–650 nm), while the halogen lights provide the longer wavelengths (around 600–1,300 nm). Extended Data Fig. 4b shows the peak power provided by the solar cells at various distances from the lights. This is measured by connecting various load resistors across the cells to obtain approximately 4.8 V (which corresponds to the peak power output) at each distance.

Electronics. To minimize complexity and facilitate rapid prototyping, the electronics design utilizes commercial off-the-shelf devices whenever possible. Small conventionally packaged transformers typically weigh around 50 mg, a substantial portion of the vehicle payload. We custom-wind a transformer using a commercial off-the-shelf inductor core (LPS3015 from Coilcraft) to the desired turns ratio and inductance. For this work, the transformer had a primary (41 AWG Magnet Wire) to secondary (51 AWG Magnet Wire) turns ratio of 1:8. To further minimize weight, wafer-level packages (in which the integrated circuits are encapsulated before being cut from the semiconductor wafer) are used whenever possible (for example, for the MCU, Q_L and Q_S). A large input capacitance ($C_{IN} > 47\,\mu F$) is necessary to decouple the input voltage from the variable load of the switching circuit; four capacitors (rated as 22 μF, US0402) connected in parallel provided sufficient charge at the input during system operation and offer the lowest mass solution. A diode D_{HS} was added in series with Q_H to ensure that conduction only occurs through the external diode when the switch is off. A complete list of components and their mass distribution can be seen in Extended Data Table 2.

Designing a single-sided PCB eliminated the need for vias, which can complicate the design and add weight. The circuit was fabricated using a direct-write photolithography and etching process on copper-clad polyimide (Pyralux AC 181200R from Dupont). To protect traces under the wafer-level-package components, silk screens (Pyralux FR1500 and Kapton HN 1 mil from Dupont) were selectively added. All components were then hand-positioned and attached using reflow soldering.

Flexboard power and efficiency. When the vehicle is operated at the conditions used for flight (approximately 195 V and 174 Hz), the piezoelectric bimorph actuators consume 28 mW (IV) and present an effective capacitive load of 48 mW (CV^2f) to the drive electronics. Using a power supply ($V_{in} = 4.8$ V), the electronics consume an average of 110–120 mW (P_{in}) when driving the vehicle at these conditions (measured using the current monitor on an external power supply). This includes an average power of 15 mW that is consumed by the microcontroller (P_{mc}) to monitor the output voltage and generate pulses. Thus, the efficiency of the drive electronics is $IV/(P_{in} - P_{mc}) \approx 28\%$. The primary loss mechanisms in this circuit, which contribute to decreased efficiency, are switching losses and losses in the magnetic components.

Drive signal analysis. Inspection of the drive signals that we apply to the integrated vehicle (Fig. 4b) shows that we achieve a peak voltage of 203 V in one half-period, and 188 V in the other. This is due to slight variations between the piezoelectric plates in the actuator, as well as in the nominal values of the resistor dividers used to monitor their voltages. We would ideally expect such signals to correspond to a flattened sine with $V_0 = 195.5$ V (and a first harmonic amplitude of 215 V; see Methods section 'Drive waveform'), and indeed the first harmonic amplitude is 212.8 V, within a couple of per cent of the expected value. This is further supported by inspecting the wing kinematics (see Supplementary Video 3), which match those achieved with a 193 V signal (212.3 V first harmonic amplitude) from external high-voltage amplifiers (PZD350A from Trek).

Centre-of-mass positioning. We place the centre of mass of the integrated vehicle in line with the centre of pressure of the wings, since this configuration minimizes the pitch and roll torques that result from manufacturing imperfections. In particular, the primary errors that lead to these torques are differences in lift between the left and right wings, lateral offsets of the mid-point of the wing strokes and non-zero mean wing drag. Changing the vertical position of the centre of mass has no effect on torques due to lateral errors in the effective centre of pressure position (which are caused by the first two error sources listed above), but torques due to wing drag asymmetries are minimized when the centre of mass is vertically aligned with the centre of pressure.

Mean power versus peak power. While the mean power required from a 4.8-V supply is 110–120 mW, we must supply a peak power of about 150–160 mW from the solar cells to achieve the same drive signal. This is due to two effects: (1) variations in the load within a flapping period cause corresponding variations in the input voltage from the cells (Fig. 4b), which also affects efficiency; (2) any reactive energy recovery from the flyback circuit cannot raise the input voltage above the solar cells' open-circuit voltage (Fig. 4c) because they would act as forward-biased diodes. For effect (2), a standard solution is the use of a blocking diode between the solar cell array and the input capacitor. A larger input capacitance would be expected to reduce the effects of effect (1).

Untethered flights. We attempted flights at several input power levels, all with the same programmed output waveform (which provided sufficient lift for sustained flight with a 60-mg solar cell array). Flights were successful (see Supplementary Videos 4 and 9) when the peak power was ≥150 mW, but not at 140 mW. Flights lasted for approximately 0.5 s before the vehicle flew outside the illuminated area and reached a maximum height of 12 cm, a peak vertical velocity of 0.36 m s⁻¹, and a peak total velocity of 0.7 m s⁻¹ (see Extended Data Fig. 6 for two flight trajectories). Although the flight at 150 mW was successful, the lift at this input power was slightly less than at higher power levels (around 280 mg versus around 290 mg). Because the power supplied by the solar cells depends on the vehicle's position and orientation, these numbers were calculated from the first three centimetres of vertical flight (see Extended Data Fig. 6), and analysis of the drive signals showed that the first harmonic was 1–2% lower than in cases when the peak power was ≥160 mW. At the operating voltage used for these flights, our lift measurement tests (Extended Data Table 1b) would suggest a lift of approximately 330 mg (the slightly lower 290 mg is due to a degradation of the vehicle's performance by about 10% between these initial lift characterization tests and the untethered flights).

The photovoltaic array and the drive electronics flexboard both have the potential to affect the flight of the vehicle through aerodynamic forces and torques. Other work has provided a detailed analysis of these effects for general 'sails'[28,34], so here we simply note estimated peak forces and torques that would be present during our flights: while the vehicle is moving upwards, there is no aerodynamic torque from the solar array or flexboard, but because there is no onboard control, slight asymmetries cause it to pitch or roll slightly. This results in lateral acceleration in addition to the desired vertical acceleration. The lateral velocity results in a torque from the drag on the flexboard, which causes the vehicle to tip further (the torque from the photovoltaic array is insufficient to prevent this because it is oriented perpendicularly to the vehicle's vertical axis). An upper bound on the forces on the photovoltaic array and flexboard is $0.5\rho_{air}Ac_d|v_{max}|^2 \approx 0.06$ mN (where the drag coefficient c_d is approximately 3.4 for our range of Reynolds numbers, the area A is approximately 2 cm², and v_{max} is the maximal observed vehicle velocity of 0.7 m s⁻¹), which is only 2% of the lift force. An upper bound for the torque from the flexboard is given by this peak drag force multiplied by the distance to the vehicle's centre of mass, or approximately 1 μN m. Looking towards future experiments with onboard control, we note that even this peak aerodynamic torque is somewhat below the control torque magnitudes we have quantified with previous two-wing vehicles and is also below the estimates for the current four-wing vehicles, as described in the Methods section 'Vehicle performance'.

System analysis. Here we consider several options for increasing the lift (F_L) of flapping-wing vehicles driven by piezoelectric actuators, while maintaining the same wingspan (S). These are to increase voltage V, to reduce the transmission ratio T and to increase the actuator width W_a. By estimating the power increase required for each of these options, we will identify the most efficient approach for lift increase.

Our analysis begins with several simplifying assumptions: in all cases, we assume that we can adjust all other vehicle parameters (for example, wing hinge stiffness) such that the system remains at the optimal operating point (for example, maximum wing pitch, the phase between wing pitch and wing stroke, and operation at the system resonance). This means that the wings' lift-to-drag ratio (F_L/F_D) would be unchanged (see the Methods section 'Vehicle design' for a description of how we adjusted the vehicle parameters to achieve this for our chosen lift-increase approach). Additionally, since we operate the vehicle at resonance, we expect the actuator force to be balanced by the wing drag. Together, this results in the following relationship: $F_L \propto F_D \propto V \times T^{-1} \times W_a$, where $V \times W_a$ is proportional to the actuator force, and the transmission ratio converts the actuator force to the force available at the wing. To achieve this change in lift force, the wing stroke speed must also change: $f\Phi = f\delta_{act}T \propto F_L^{0.5}$ (where f is the flapping frequency, Φ is the stroke angle amplitude and δ_{act} is the amplitude of actuator deflection). To maintain a fixed vehicle lifetime, we keep the peak actuator strain, and thus δ_{act}, unchanged. Thus, $f \propto V^{0.5}T^{1.5}W_a^{0.5}$. This allows us to compute the power usage, which consists of two components: the real power $P_{in,R} = IV$ and the capacitive power $P_{in,C} = CV^2f$ (the latter is the power required to charge and discharge a capacitor to an energy of $0.5CV^2$ at a frequency f with no energy recovery). The real power is within 10% of the mechanical output power, so we have $P_{in,R} \approx P_{out} = \pi f\delta_{act}F_{act}$ (where $F_{act} \propto$

$W_a V$ is the amplitude of the actuator force). Thus, $P_{in,R} \propto V^{1.5} \times T^{-1.5} \times W_a^{1.5}$ and $P_{in,C} \propto V^{2.5} \times T^{-1.5} \times W_a^{1.5}$. From these expressions, we see that $P_{in,R}$ scales in the same way whether we increase V, decrease T or increase W_a. However, $P_{in,C}$ is much worse if we increase V. In addition, the circuits used to convert low-voltage inputs to high-voltage drive signals suffer additional efficiency losses at higher voltages, and have maximum operating voltages around 200 V for the components we are using. Although reducing T and increasing W_a result in the same scaling for lift and power, increasing W_a results in a heavier vehicle. Hence, we focus on reducing the transmission ratio (we note that the stroke amplitude decreases in this scenario; eventually this is expected to reduce the lift-to-drag ratio of the wings, due in part to their finite width, but we have not yet observed this effect).

The above methods can be used to increase lift, but we also need to improve efficiency (that is, the ratio of lift generated to power used). As noted in the main text, we can achieve this by flapping a larger area of wings more slowly, since mechanical power equals force times velocity. However, we cannot simply increase the size of the wings, because that would require a larger actuator force (the required actuator force is proportional to the wing drag times the wing length). We could increase the width of the wings, but that aspect ratio affects the lift-to-drag ratio, and its optimization is beyond the scope of this paper. However, consider that in the previous vehicle[5] SDAB1, the wing stroke is approximately 90 degrees peak to peak, which means that about half of the circle swept out by the wings is unused. This means that our best option for increasing the wing area is simply to add a second pair of wings in this available space. Also, to put this in a more general context, we note that although the stroke angle is limited for this vehicle by the strain limit of the piezoelectric actuators, even if we could double the strain limit, it is still preferable to use four wings (along with half the transmission ratio and half the voltage). That is, if we used an actuator with twice the achievable strain to double the wing stroke, we would achieve the same thrust at half the frequency. This would not affect the real power consumption, but would halve the capacitive power. However, if we instead halve the transmission ratio and keep the same wing stroke and frequency, we can achieve the same thrust at half the voltage. This still has no effect on the real power, but it reduces the capacitive power by a factor of four. Then we can still add in a second pair of wings for a further 30% reduction in both real and capacitive power.

To illustrate these predicted effects for vehicle thrust and efficiency on system level performance, in Extended Data Fig. 7 we condense the multi-dimensional problem (transmission ratio, number of wings, actuator width and the overall vehicle scaling) as follows. (1) We hold voltage and actuator strain constant; (2) we consider two transmission ratios, the value used in SDAB1 and $1/1.26\times$ that value; (3) the number of wings is either two or four; (4) we consider several choices of actuator width, $1\times$, $2\times$ and $3\times$ that used in SDAB1; and (5) we treat overall vehicle scaling (relative to SDAB1) as a continuous parameter. Here 'overall vehicle scaling' means scaling everything equally in all three dimensions by a factor n. For example, wing length, width and thickness are scaled by n and actuator mass is scaled by n^3 (in practice, we scale only the actuator width by n^3, and do not change T, to achieve the same result). We aim to illustrate two key points: that four wings are better than two regardless of any of the other parameters, and that we want to minimize the power required for a given wingspan when we are using solar cells for the power source. We also use this analysis to identify a slightly more optimal overall vehicle size for future work.

In particular, the top row of Extended Data Fig. 7 shows the power required to fly (P_n) and the power available at 1 Sun (P_a). $P_n = P_{L,0}\widetilde{T}^{-1.5}(0.5N)^{-0.5}n^2 + P_m$ and

$P_a = (0.9n^2\widetilde{T}^{-1}F_{L,0}/1.1 - n^3 M_{aa} - M_{fb} - M_o) \times P_d$, where n is the overall vehicle scaling, $\widetilde{T}$ is the relative transmission ratio (compared with SDAB1) and $F_{L,0} = 270$ mg is the lift of SDAB1. M_{aa} is the mass of actuators and airframe (80 mg when $\widetilde{T} = 1$ and 90 mg when $\widetilde{T} = 1/1.26$; reducing T requires heavier alumina-bridge actuators owing to the increased forces; see Methods section 'Vehicle design'), $M_{fb} = 91$ mg is the mass of the flexboard, $M_o = 11$ mg is the mass of the posts and bondic that affix the solar cells and flexboard to the vehicle (4 mg post, 7 mg bondic), $P_d = 0.76$ W g^{-1} is the power density of the solar cells, $P_{L,0} = 95$ mW is the power to fly SDAB1 (including drive electronics losses; the mean vehicle power P_{IV} was 28 mW), N is the number of wings and $P_m = 15$ mW is the power consumption of the microcontroller. We note that P_a is proportional to the payload available for a power supply (the steps in the plot are due to the need for an even number of solar cells). These equations make the following assumptions: that the required lift is 1.1 times the total vehicle mass, that the lift force has a 10% degradation from initial characterization (often 5–10% in practice), that the flexboard has a fixed weight and efficiency for the range of powers covered[19] and that actuator strain and drive voltage are kept fixed for all vehicles.

The second row of Extended Data Fig. 7 shows the ratio of P_n to P_a, or the average light intensity required in number of Suns (this is equivalent to the minimum viable power density of the power supply, in increments of 0.76 W g^{-1}). Here we can more clearly see that vehicles with four wings require fewer Suns (that is, lower power density) than those with two wings, regardless of transmission ratio, actuator width or overall vehicle scale.

Our main concern for achieving untethered flight is reducing the number of Suns required, but we note that similar values can be achieved for a range of actuator widths (the black, red and blue curves in Extended Data Fig. 7). However, since we are focusing on the use of solar cells in this work, we want to minimize $A_s/\pi(0.5S)^2$ (the ratio of solar cell area, A_s, to the area 'swept' by the wings, $\pi(0.5S)^2$, where S is the wingspan), so as to minimize the impact of the solar cells on airflow (that is, we do not want the solar cells to be too large in comparison with the wings). The bottom row of Extended Data Fig. 7 shows the strong effect that actuator width has on this ratio, and suggests that we want the narrowest actuators that still allow the vehicle to fly with a given number of Suns. (We note that if using a battery, we might want the opposite, because a battery could be placed within the vehicle, and its power density generally increases with size.)

For this work, we opted to use a vehicle with the same wingspan as SDAB1. Dots in the figure indicate values for that vehicle, and our predictions for the new vehicle, with a predicted reduction in the required average light intensity from five to seven Suns to approximately two Suns. The plots in Extended Data Fig. 7 suggest that a vehicle scaled up by roughly $1.26\times$ should reduce this further, to about 1.5 Suns, and this will be pursued in future work.

Data availability

The data that support the findings of this study are available from the corresponding author upon reasonable request.

34. Fuller, S. B. et al. Stabilizing air dampers for hovering aerial robotics: design, insect-scale flight tests, and scaling. *Auton. Robots* **41**, 1555–1573 (2017).

35. Jayaram, K., Jafferis, N. T., Doshi, N., Goldberg, B. & Wood, R. J. Concomitant sensing and actuation for piezoelectric microrobots. *Smart Mater. Struct.* **27**, 065028 (2018).
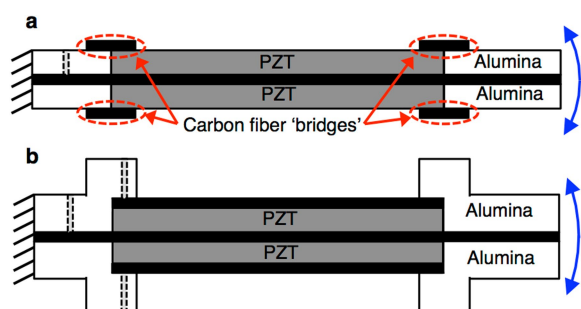
Extended Data Fig. 1 | Actuator cross-sectional diagrams. a, The actuators developed in ref. [18]. **b**, The alumina-reinforced actuators used in this work. The blue arrows indicate the bending direction of the actuators.
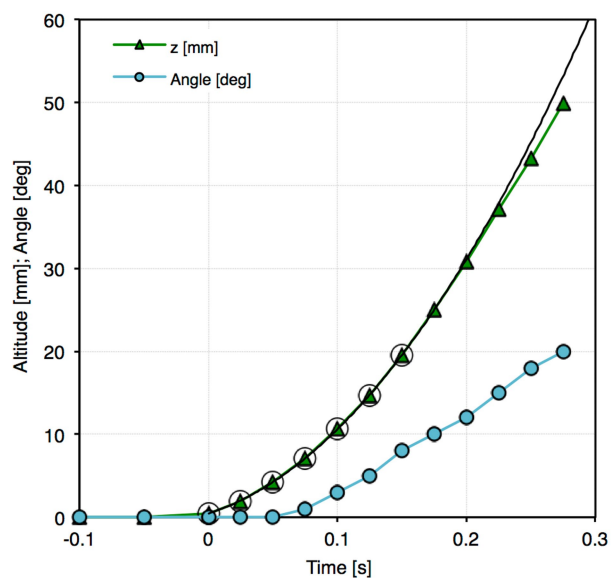
Extended Data Fig. 2 | Lift force measurement via vertical acceleration. The vehicle's altitude versus time when operated at 210 V, 165 Hz, and carrying a payload of 245 mg (for a total mass of 335 mg). The voltage is increased from zero to 210 V from $t = -0.1$ s to $t = 0$ s, and remains at 210 V for the remainder of the trial. The curvature of this trajectory shows that the lift is 370 mg for this operating condition. The lift is calculated from a least-squares fit to the circled data points, which occur while the vehicle's deviation from vertical (labelled 'angle' in the plot) is small enough to cause errors <1%; correcting for the angle error gives the same lift value over the entire flight time.
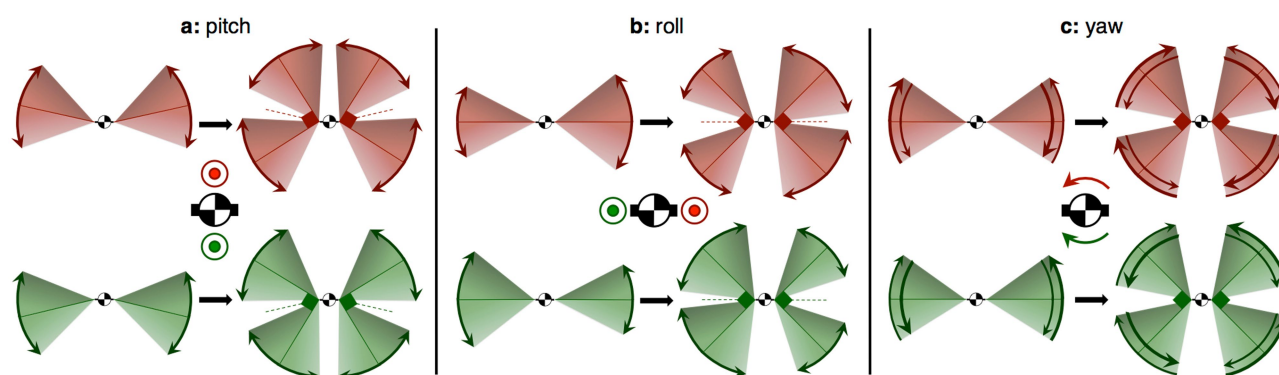
Extended Data Fig. 3 | Illustration of torque implementation. a–c, Pitch torque (**a**), roll torque (**b**) and yaw torque (**c**) (all depicted with 'top-down' views of the wing strokes), in the X-Wing versus the previous two-wing design. The red and green squares in the X-Wing design indicate that each pair of wings is fixed at 90 degrees apart. Although the four-wing design brings the mean centre of pressure of each wing pair closer to the body for pitch and roll (indicated by the length of the dashed lines), it also produces greater forces for the same flapping motion, allowing for similar control authority.
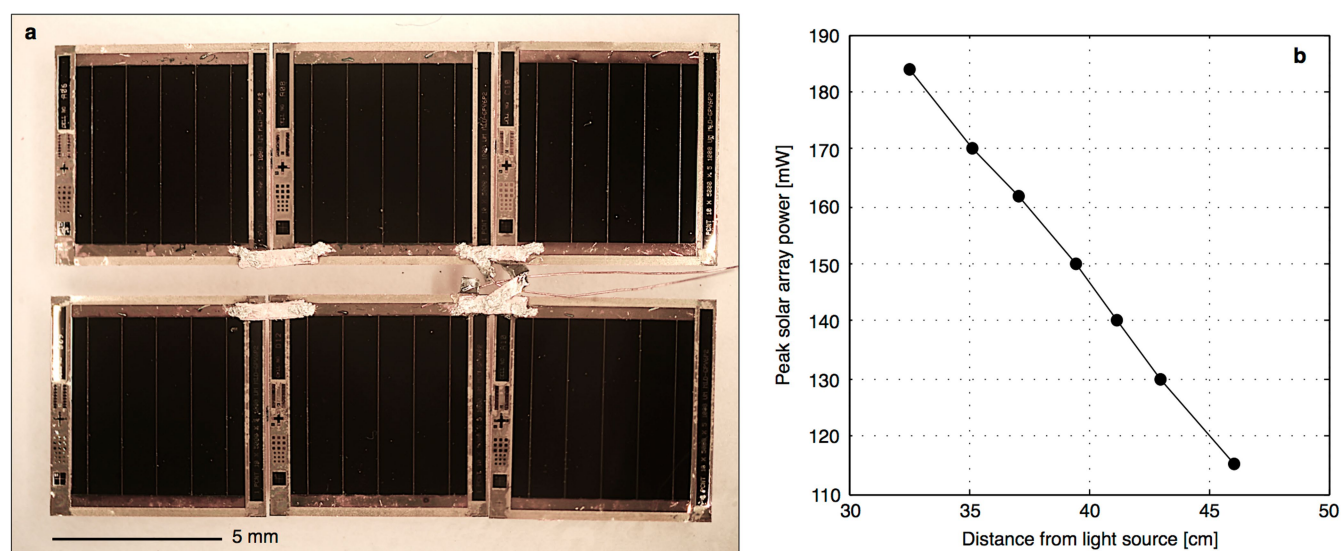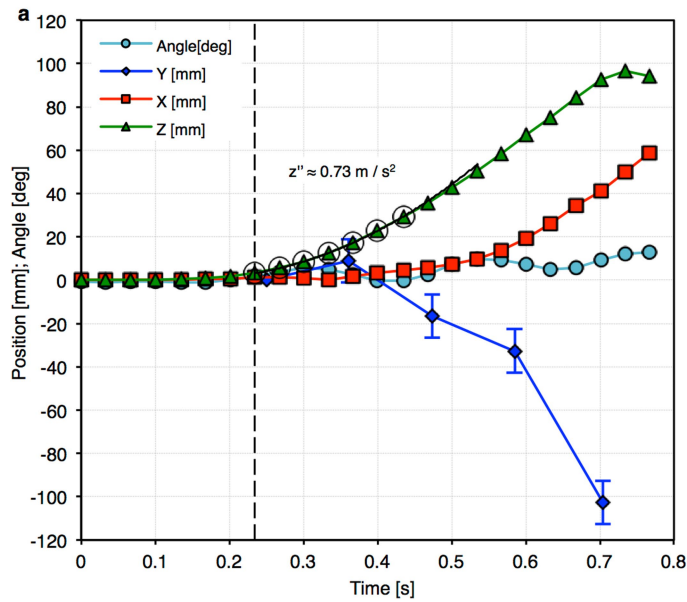
Extended Data Fig. 4 | Power supply. a, Six-cell photovoltaic array. **b**, Plot of the power obtained from this solar array at varying distances from our light source (the measurement precision is approximately ±5 mW). The power at 1 Sun is approximately 46 mW.
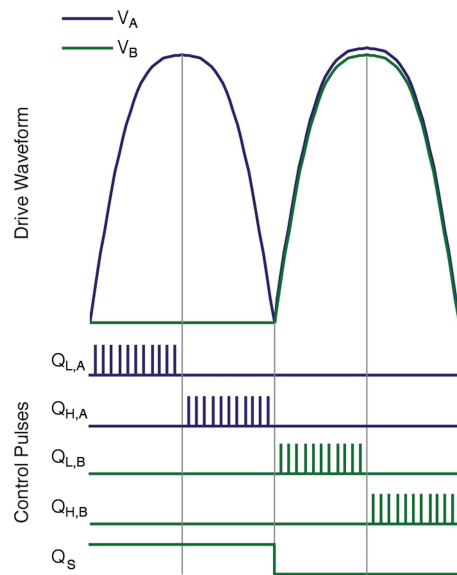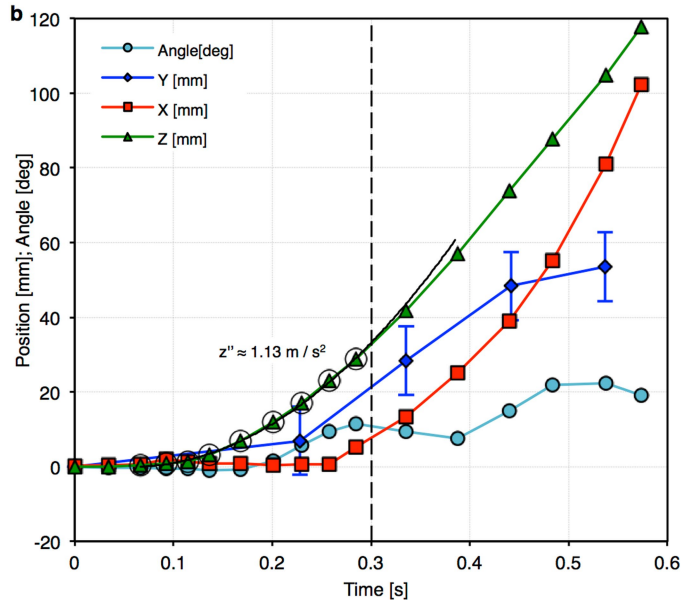
**Extended Data Fig. 5 | Drive waveform switching control diagram.**

Extended Data Fig. 6 | Trajectories for the untethered flights. Z is altitude, X and Y are lateral displacements, and 'Angle' is the projection of the vehicle's orientation onto the X–Z plane (that is, the camera view), with vertical being zero. The light turns on at $t = 0$, and the vertical dashed line indicates when it has reached full intensity. **a**, The flight shown in Supplementary Video 9 (the lowest-power flight).
b, The flight shown in Supplementary Video 4. Depth (Y) is estimated by measuring the fractional change in the peak width of the flexboard as our integrated vehicle spins about the yaw axis (that is, twice every yaw period, we measure the width of the flexboard), along with the starting distance from the vehicle to the camera (approximately 90 cm). The error bars on Y are due to the pixel resolution error (± 0.2 mm) amplified by the ratio of the camera distance to the flexboard width. The lift force is estimated from the vertical acceleration (z'') of the vehicle during the first 3 cm of vertical flight (indicated by the circled data points), before the vehicle has noticeably tilted or moved laterally (note that for the flight in **b**, our lift estimate is based on data before the light has reached full intensity, because the vehicle has already moved and tilted noticeably by then).
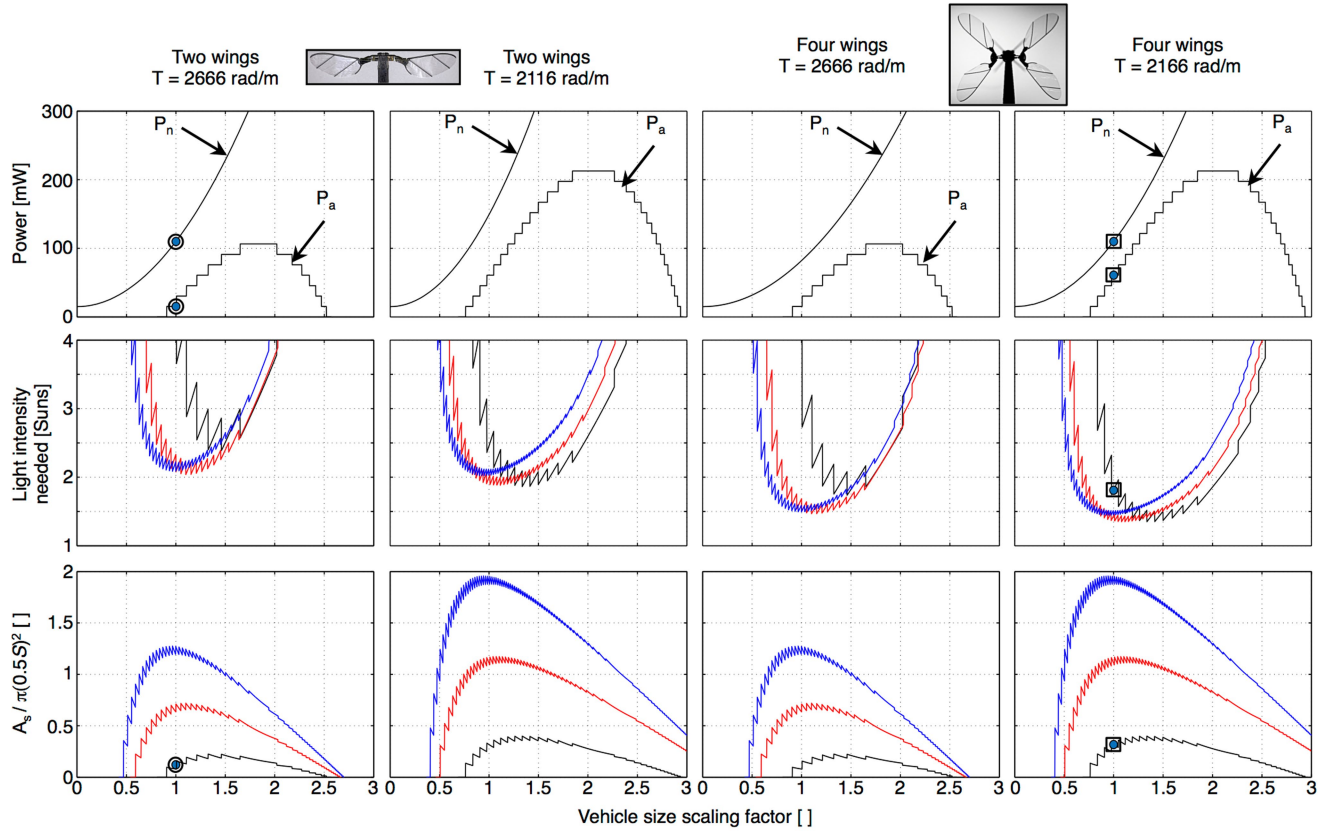
Extended Data Fig. 7 | System trade-off analysis. This series of plots compares predictions for the required power (P_n) and the power available at 1 Sun (P_a) (power density 0.76 W g^{-1}) (top row); the mean light intensity required to fly (in number of Suns) (middle row); and the area of solar cells that can be carried (A_s) divided by the area 'swept' by the wings ($\pi(0.5S)^2$) (bottom row). These quantities are plotted as functions of overall vehicle scaling for vehicles with two or four wings and two different transmission ratios. Plots are shown for three actuator widths: $1\times = 1.125$ mm (black), $2\times = 2.250$ mm (red) and $3\times = 3.375$ mm (blue). The circled and squared dots correspond to predictions for SDAB1[5] and the vehicle described in this work, respectively. The steps in the plots are due to the discrete size of available solar cells.

Extended Data Table 1 | Vehicle characterization

a

Parameter	Change
T	0.79×
K_{act}	1.28×
κ_T	1×
K_{tot}	0.93×
$I_{yy,frame}$	0.75×
$I_{yy,mem}$	1×
$I_{yy,tot}$	0.8×
N	2×
M_{eff}	1×
f_s	0.96×
κ_{wh}	0.75×
$I_{xx,frame}$	0.75×
$I_{xx,mem}$	1×
$I_{xx,tot}$	0.8×
f_p	0.97×

b

Parameter	SDAB1$_A$	SDAB1$_B$	New Vehicle		
$V_{pp,flat}$	185 V	190 V	190 V	200 V	210 V
f	172 Hz	165 Hz	173 Hz	170 Hz	165 Hz
Φ_{pp}	95.5°	98°	68.8°	77.5°	88°
$v_{eff,max}$	9.01 m/s	8.87 m/s	6.39 m/s	7.08 m/s	7.80 m/s
ϵ/ϵ_0	1	1.03	0.91	1.02	1.16
F_L	270 mg	270 mg	325 mg	340 mg	**372 mg**
$C_l/C_{l,0}$	1	1.03	1.19	1.02	0.92
$C_d/C_{d,0}$	1	1.06	1.31	1.12	0.97
$L2D/L2D_0$	1	0.97	0.91	0.91	**0.95**
$P_{calc, IV}$	28 mW	28 mW*	26 mW	31 mW	35 mW
P_{calc,CV^2f}	48 mW	48 mW*	50 mW	55 mW	59 mW
η/η_0[†]	1	0.99	1.29	1.15	1.09
"Ideal" η/η_0[‡]	1	1.02	1.41	1.27	1.16

a, Vehicle parameter changes (compared with SDAB1). **b**, Vehicle performance. Power values ($P_{calc,IV}$ and $P_{calc,CV2f}$) are calculated based on actuator capacitance and wing stroke velocity[35]. $V_{pp,flat}$ is the peak-to-peak voltage for the flattened sinusoid drive waveform. L2D, lift-to-drag ratio.
*Values that were also measured directly for verification.
[†]$\eta \equiv F_L/P_{IV}$.
[‡]'Ideal' $\eta/\eta_0 = v_{eff,0}/v_{eff}$. I_{frame} and I_{mem} are the inertias of the carbon fibre frame (leading edge and spars) and polyester membrane, respectively. All other parameters are defined in the text.

Extended Data Table 2 | Components of the signal-generation electronics and their corresponding masses

Component	Schematic Notation	Part	Supplier	Mass [mg]
Transformers	L_A, L_B	LPS3015	Coilcraft	32
Low-side Switch	$Q_{L,A}$, $Q_{L,B}$	EPC2036	Efficient Power Conversion Corporation	2.6
High-side Switch	$Q_{H,A}$, $Q_{H,B}$	MSD42SWT1G	ON Semiconductor	11.4
Secondary Switch	Q_S	EPC2012	Efficient Power Conversion Corporation	2.8
Input Capacitor	C_{IN}	22µF C0402 (×4)	Samsung Electromechanics	24
Diodes	$D_{L,A}$, $D_{L,B}$, $D_{H,A}$, $D_{H,B}$, $D_{HS,A}$, $D_{HS,B}$	BAS521LP	Diodes Incorporated	5.4
Resistors	$R_{1,A}$, $R_{1,B}$	5M R0402	Ohmite	1.2
	$R_{2,A}$, $R_{2,B}$	25K R0201	Samsung Electromechanics	0.5
Microcontroller	MCU	ATTiny20	Atmel	3
Board, solder, silkscreen				8
			Total Mass:	91